ACS OMEGA

http://pubs.acs.org/journal/acsodf

Article

One-Step Hydrothermal Synthesis of Nitrogen-Doped Reduced Graphene Oxide/Hausmannite Manganese Oxide for Symmetric and Asymmetric Pseudocapacitors

Katlego Makgopa,* Mpho S. Ratsoma, Kumar Raju, Letlhogonolo F. Mabena, and Kwena D. Modibane*

Cite This: *ACS Omega* 2021, 6, 31421−31434

Read Online

ACCESS | Metrics & More | Article Recommendations

ABSTRACT: In this paper, the pseudocapacitive performance of nitrogen-doped and undoped reduced graphene oxide/tetragonal hausmannite nanohybrids (N-rGO/Mn_3O_4 and rGO/Mn_3O_4) synthesized using a one-pot hydrothermal method is reported. The nanohybrid electrode materials displayed exceptional electrochemical performance relative to their respective individual precursors (i.e., reduced graphene oxide (rGO), nitrogen-doped reduced graphene oxide (N-rGO), and tetragonal hausmannite (Mn_3O_4)) for symmetric pseudocapacitors. Among the two nanohybrids, N-rGO/Mn_3O_4 displayed greater performance with a high specific capacitance of 345 F g^{-1} at a current density of 0.1 A g^{-1}, excellent specific energy of 12.0 Wh kg^{-1} (0.1 A g^{-1}), and a high power density of 22.5 kW kg^{-1} (10.0 A g^{-1}), while rGO/Mn_3O_4 demonstrated a high specific capacitance of 264 F g^{-1} (0.1 A g^{-1}) with specific energy and power densities of 9.2 Wh kg^{-1} (0.1 A g^{-1}) and 23.6 kW kg^{-1} (10.0 A g^{-1}), respectively. Furthermore, the N-rGO/Mn_3O_4 nanohybrid exhibited an impressive pseudocapacitive performance when fabricated in an asymmetric configuration, having a stable potential window of 2.0 V in 1.0 M Na_2SO_4 electrolyte. The nanohybrid showed excellent specific energy and power densities of 34.6 Wh kg^{-1} (0.1 A g^{-1}) and 14.01 kW kg^{-1} (10.0 A g^{-1}), respectively. These promising results provide a good substance for developing novel carbon-based metal oxide electrode materials in pseudocapacitor applications.

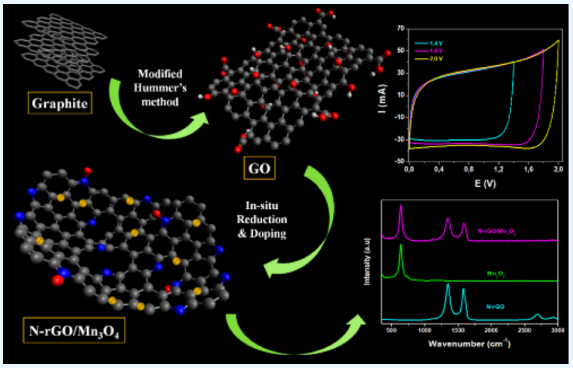

1. INTRODUCTION

Electrochemical energy storage devices have emerged as the key technological solution to the rising energy demand and the limited availability or harsh environmental impact of fossil fuels.[1,2] Such energy storage devices should be able to deliver robust power and energy outputs while being able to still retain their stability and efficiency after long charge−discharge cycles. The inherent high efficiency of an electrochemical energy storage device and its capability to store the harnessed energy from renewable energy sources such as solar, wind, etc., has drawn much attention in the current energy research.[3,4] Among the electrochemical energy storage devices, supercapacitors (SCs) have proved to possess such characteristics as described above and hence continue to receive much attention from the scientific research community.[5] The primary goal for the choice of supercapacitors as a device of choice is to design and develop a new type of technology that surely surpasses and bridges the gap between batteries (famous for their high energy densities) and conventional capacitors (famous for their high power densities).[6] Apart from the current trend of supercapacitors being used as a supportive energy storage device in renewable energy sources, these devices are also mostly used in a variety of applications such as hybrid electric vehicles (HEVs), portable electronic devices, and backup power memory.[7] Furthermore, the charge storage mechanism in SCs is different from the one in batteries. There are three classes of SCs based on their charge storage mechanisms: all-carbon-based electrical double-layer capacitors (EDLCs), pseudocapacitors, and hybrid capacitors.[8−12] The EDLCs can store energy by charge separation at the electrode/electrolyte interface, whereas the pseudocapacitors use electroactive metal oxide and/or conducting polymers to store energy by redox or Faradaic processes. It was seen that the hybrid capacitors incorporate both the Faradaic reactions (pseudocapacitance) and the non-Faradaic reactions (EDLCs).[8−12]

The pseudocapacitor and the hybrid capacitor are reported to exhibit superior capacitance in comparison with the EDLC, with the hybrid capacitor ranking high. Nonetheless, it is documented that the physicochemical properties of the

Received: May 2, 2021
Accepted: September 24, 2021
Published: November 15, 2021

Scheme 1. Illustration of the One-pot Synthesis of a N-rGO/Mn_3O_4 Nanohybrid

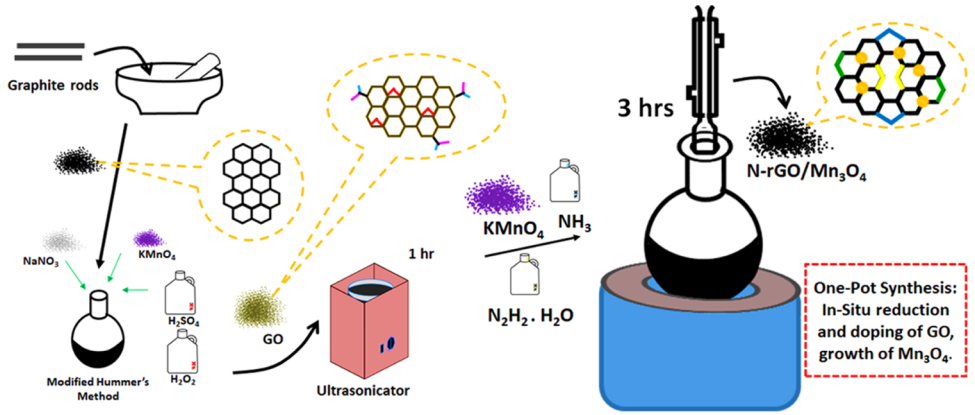

working-electrode materials affect the performance of supercapacitors.[12] Nevertheless, one of the major shortcomings of the pseudocapacitive electrode materials as compared to counterpart electrode materials is their poor rate-capability as a result of poor conductivity. In an effort to develop a high capacitive supercapacitor, nanostructured carbon materials are incorporated with electroactive species such as metal oxides or conducting polymers to achieve improved electrochemical performance.[11] The intensive use of the nanostructured carbon materials is owing to their exceptional properties, including a higher specific surface area of around 2000 $m^2\ g^{-1}$, nontoxicity, good chemical stability, natural abundance, and excellent electronic conductivity. Among several carbon nanomaterials discovered and explored for energy storage applications in supercapacitors, graphene has shown to be the leading emerging carbon nanomaterials due to its intriguing properties, such as highly tunable surface area, outstanding electrical conductivity, good chemical stability, and excellent mechanical behavior.[11,13] Due to challenges in the bulk synthesis of graphene, reduced graphene oxide (rGO) has been opted as the preferred choice of electrode material for the development of supercapacitor devices.

The interest in using transition-metal oxides (TMOs) as electrode materials for SC applications has increased.[14] Among TMOs, manganese oxides, Mn_xO_y, appeared to be the promising electrode material for pseudocapacitors because of their interesting properties, including cost-effectiveness, great theoretical specific capacitance, extraordinary theoretical surface area ($\geq$1370 $m^2\ g^{-1}$), and excellent electrochemical reversibility.[15−17] The Mn_3O_4 is one of the most stable oxides in the manganese oxide family and has single black manganese with controllable microstructures at room temperature. This makes it an ideal material for supercapacitors in terms of cost-effectiveness, high specific capacitance, and being environmentally friendly. However, the poor electronic conductivity and manganese dissolution of Mn_3O_4 lead to poor cycle stability, which restricts its progress in SC applications.[5,18] Therefore, it is essential to improve the electronic conductivity of Mn_3O_4 by the addition of any conductive additives such as OLCs, CNTs, graphene, and rGO.[5,19,20] Jiang and Kucernak[21] reported on a Mn_3O_4 thin-film electrode material with a specific capacitance of 92 and 58 F g^{-1} in aqueous electrolytes and organic electrolytes, respectively. However, the combination of Mn_3O_4 with MWCNT (Mn_3O_4/MWCNT composite) displayed a maximum specific capacitance of 330 F g^{-1}.[22] In contrast, the Mn_3O_4/graphene composite exhibited a specific capacitance of 175 F g^{-1},[23] while Mn_3O_4 decorated with an onionlike carbon (OLC/Mn_3O_4 nanohybrids) in a symmetric configuration exhibited a specific capacitance and maximum energy of 195 F g^{-1} and 4.3 Wh kg^{-1}, respectively.[19] The power density of this nanohybrid was reported to be 52 kW kg^{-1}. The OLC/Mn_3O_4 nanohybrids also showed a maximum energy density of 19 Wh kg^{-1} at 0.1 A g^{-1} current density and a power density of 45 kW kg^{-1} at 10 A g^{-1} current density during an asymmetric configuration.[19] The functionalization of graphitic carbon materials introduces lattice defects that improve the electronic and catalytic activity of the graphitic material, resulting in better interactions with the electrolytes and thus enhancing the wettability of the material.[24−26] On the other hand, carbon-based materials doped with nitrogen, boron, phosphorus, and sulfur heteroatoms in different combinations result in the superior performance of energy storage devices.[27] In this study, we have explored the facile synthetic process (one-pot synthesis) for tuning the electronic structure of rGO by introducing the N-atoms, followed by anchoring of the Mn_3O_4 onto the surface of the N-rGO to form a nanohybrid with improved conductivity. The as-prepared N-rGO/Mn_3O_4 nanohybrid exhibited excellent pseudocapacitive properties such as specific capacitance, rate performance, and cycle stability with respect to the rGO/Mn_3O_4 nanohybrid and their precursors.

2. EXPERIMENTAL SECTION

2.1. Preparation of Electrode Materials. *2.1.1. Synthesis of Graphene Oxide (GO).* Graphene oxide was prepared using the exfoliation of graphite according to a modified Hummers' method.[28,29] Briefly, a graphite rod (6.15 mm (diameter) × 152 mm (long), 99.9995% (metal basis), AGKSP grade, ultra "F" purity) acquired from Alfa Aesar (a Johnson Matthey Company) was ground to a fine powder using a pestle and mortar, followed by filtering through a 210-micron sieve. The filtered graphite powder and 1.0 g of $NaNO_3$ (1:1 mass ratio) were weighed into a 250.0 mL beaker, and 50.0 mL of concentrated H_2SO_4 was gradually introduced to the mixed powder at 0 °C; subsequently, 6.0 g of $KMnO_4$ was added. The solution mixture was then stirred constantly for 1 h at 25 °C. The mixture was slowly transferred into a 400.0 mL beaker containing 200 mL of deionized water, and after 15 min, a 30% H_2O_2 solution was added to the reaction mixture under constant stirring until the gas evolution ceased. The reaction mixture was then filtered, and the precipitate was washed repeatedly with 5% HCl solution and deionized water. Finally,

https://doi.org/10.1021/acsomega.1c02302
ACS Omega 2021, 6, 31421−31434

the powders were dried overnight at 60 °C in an oven to obtain the yellow-brown solid of GO.

2.1.2. Syntheses of N-rGO/Mn_3O_4 and rGO/Mn_3O_4 Nanohybrids and Other Precursors. The preparation of N-rGO/Mn_3O_4 and rGO/Mn_3O_4 nanocomposites followed a facile one-pot hydrothermal reaction (see Scheme 1). For N-rGO/Mn_3O_4, GO (0.31 g) was dispersed in 600 mL of deionized water and ultrasonicated for 1 h. The solution was then transferred into a 1.0 L round-bottomed flask, and about 150 mL of an aqueous solution of 1 mg/mL $KMnO_4$ was added to the flask. Then, 3.0 mL of 25% NH_3 solution was added to the mixture under constant stirring, and subsequently, 3.0 mL of 99% hydrazine hydrate was slowly added to the reaction mixture, and ultimately the solution was refluxed for 3 h at 95 °C. The black color solution was then filtered, and the product was washed with a copious amount of water and ethanol and then dried overnight in an oven to afford N-rGO/Mn_3O_4. The synthesis of rGO/Mn_3O_4 followed the abovementioned process in the absence of NH_3. The syntheses of N-rGO and rGO followed similar conditions that were used in the abovementioned procedure, in the absence of $KMnO_4$ (N-rGO) and NH_3 (rGO). The synthesis of hausmannite Mn_3O_4 followed the above procedure in the absence of GO and NH_3.[30]

2.2. Microscopic and Spectroscopic Evaluation. The microscopic properties of the synthesized materials were probed using a scanning electron microscope (SEM; JSM-7500F, JEOL, Japan) fitted with energy-dispersive X-ray spectroscopy (EDS; for elemental analysis and mapping). The structural elucidation and elemental composition analyses were obtained using an X-ray diffractometer (XRD; Rigaku Ultima IV) equipped with Ni-filtered Cu Kα radiation (λ = 1.541841 A) operating a copper tube at 30 kV and 40 mA. A Raman WITec Confocal Microscope (WITec α 300 R, Germany) with a laser wavelength of 532 nm, a laser power of 4 mW, and a spectral acquisition time of 120 s and an X-ray photoelectron spectroscope (XPS; PHI 5000 Versaprobe-Scanning ESCA Microprobe instrument, ESCA) were used.

2.3. Electrode Fabrication. Fabrication of the electrodes was done by mixing the active materials (80%) with carbon black (15%) and poly(vinylidene fluoride) (5%) using a pestle and mortar, followed by the addition of anhydrous N-methyl-2-pyrrolidone (NMP) to make a homogeneous paste. Poly(vinylidene fluoride) and carbon black functioned as the binder and conductive materials, respectively. Nickel foam pretreated with 1.0 M HCl, washed with deionized water, and dried under vacuum was used as a current collector. All of the prepared electrodes were dried at 80 °C overnight in a vacuum oven. The electrochemical cell was constructed in a two-electrode system using a Swagelok cell with electrodes assembled in respective symmetric and asymmetric configurations. A porous glass fiber (Whatman Grade GF/D glass microfiber filters, Sigma-Aldrich) and 1.0 M Na_2SO_4 solution were employed as the separator and electrolyte, respectively.

2.4. Electrochemical Evaluation. A Bio-Logic VMP 300 potentiostat/galvanostat (EC-Lab v10.40 software) was used for the electrochemical evaluations of the synthesized electrode materials. Cyclic voltammetry (CV) analyses were recorded at various scan rates between 2 and 100 mV s^{-1} in a potential range of 0 to 1.0 V. Galvanostatic charge−discharge (GCD) analyses were recorded from various current densities between 0.1 and 10 A g^{-1}. Electrode resistance properties were probed using the electrochemical impedance spectroscopy (EIS) technique employing a frequency range from 0.1 Hz to 100 kHz under an open-circuit potential, and the data were fitted using the Z-fit tool. The stability evaluation of the electrodes was obtained via voltage holding for 10 h (times 5) at 1.1 V, with subsequent GCD analysis between a potential window of 0.0 and 1.1 V (at 2.0 A g^{-1}). The electrochemical performance parameters (i.e., specific capacitance (C_{sp}), maximum specific power density (P_{max}), and specific energy density (E_{sp})) of the electrode materials were derived from GCD curves by following eqs 1−5.[31]

$$C(\mathrm{F}) = \frac{i}{\Delta V/\Delta t} \tag{1}$$

$$C_{sp}(\mathrm{F/g}) = \frac{4\cdot C}{m} \tag{2}$$

$$P_{max}(10^3\,\mathrm{W/kg}) = \frac{V^2}{4mR_s} \tag{3}$$

$$E\left(\frac{1}{3.6}\,\mathrm{Wh/kg}\right) = \frac{CV^2}{2m} \tag{4}$$

$$R_s(\Omega) = \frac{\Delta V_{IR}}{2i} \tag{5}$$

where C represents the cell capacitance in Farads (F), i represents the applied current in amperes (A), V represents the potential in volts (V), t represents the time in seconds (s), m is the total mass of the electrodes in grams (g), R_s represents the equivalent series resistance (ESR) in ohms (Ω) determined from the IR drop, and ΔV_{IR} represents the drop in voltage of the first two points on the discharge curve.

The evaluation of the electrochemical performance in an asymmetric configuration was achieved using activated carbon (AC) as the negative electrode and the N-rGO/Mn_3O_4 nanohybrid as the positive electrode. The mass balancing of the individual electrodes using a three-electrode system (i.e., $m_+/m_- = 0.34$), as an essential step in the optimization of the cell voltage to maintain equal charges, was achieved using eq 6

$$\frac{m_+}{m_-} = \frac{C_{sp-}}{C_{sp+}} \times \frac{\Delta E_-}{\Delta E_+} \tag{6}$$

where m_+ and $m-$ represent the mass, C_{sp+} and C_{sp-} represent the specific capacitance, and ΔE_+ and ΔE_- represent the potential window of the individual positive and negative electrode, respectively.

3. RESULTS AND DISCUSSION

3.1. Formation Mechanism: One-Pot Synthesis of the N-rGO/Mn_3O_4 Nanohybrid. Scheme 1 demonstrates the formation mechanism of the N-rGO/Mn_3O_4 nanohybrid. The presence of NH_3 facilitates the doping of N-atoms on the carbon material, while the $KMnO_4$ acts as the precursor of manganese oxide to form Mn_3O_4 nanoparticles. The N-doping and the reduction of both Mn^{7+} to $Mn^{3+/4+}$ and GO to rGO are done in situ via the presence of hydrazine, which is a strong reducing agent. The formation of rGO/Mn_3O_4 took place using a similar route but in the absence of NH_3.

3.2. Scanning Electron Microscopy (SEM) Analysis. To understand the surface morphology of the synthesized materials, SEM analysis was performed, as shown in Figure 1, which depicts microscopic images of (a) N-rGO/Mn_3O_4,

https://doi.org/10.1021/acsomega.1c02302
ACS Omega 2021, 6, 31421−31434

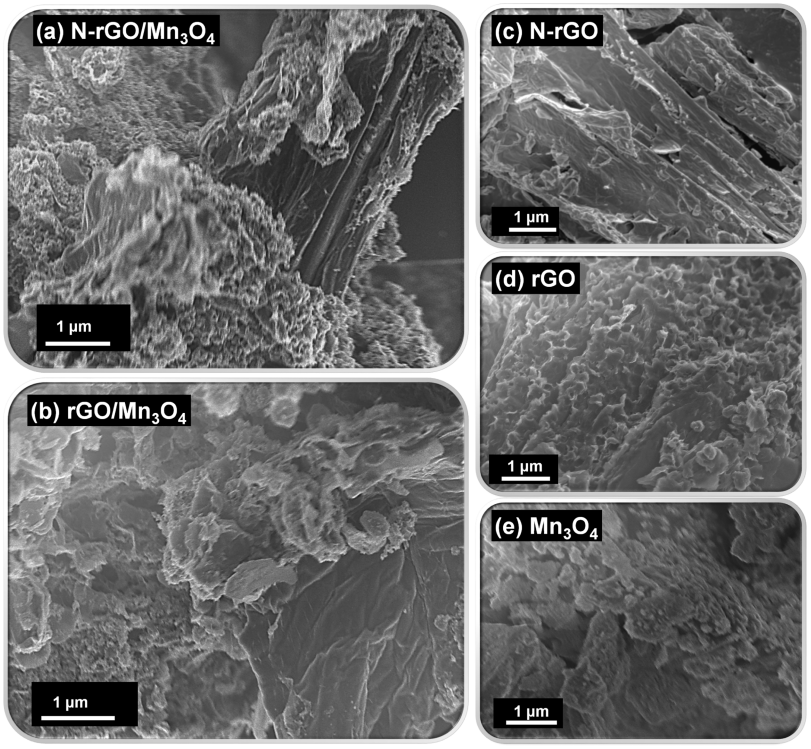

Figure 1. SEM images of (a) N-rGO/Mn_3O_4, (b) rGO/Mn_3O_4, (c) N-rGO, (d) rGO, and (e) Mn_3O_4.

(b) rGO/Mn_3O_4, (c) N-rGO, (d) rGO, and (e) Mn_3O_4. The crystalline Mn_3O_4, the wrinkled rGO, and the wrinkled and chaotically flaky N-rGO can be observed in the images of Figure 1f rGO/Mn_3O_4 and (g) N-rGO/Mn_3O_4. These traits can be correlated back to those of the individual N-rGO, rGO, and Mn_3O_4 in Figure 1c−e, respectively, indicating a successful decoration of Mn_3O_4 nanoparticles on rGO and N-rGO. The introduction of nitrogen onto the structure of rGO resulted in the chaotic flaky morphology of N-rGO.

3.3. XRD, Raman, and EDX Analyses. The structural and chemical constituency of the as-prepared nanomaterials was investigated using the XRD, Raman, and EDX characterization techniques. Diffraction patterns of graphite, GO, rGO, and N-rGO in Figure 2a show a graphitic peak at 2θ = 26.43° corresponding to the (002) diffraction plane with an interlayer spacing of about 3.37 Å. The same peak can be observed from the spectra of N-rGO/Mn_3O_4 and rGO/Mn_3O_4 in Figure 2b. The *d*-spacing value is approximate to that reported in the literature of 3.35 Å for graphitic carbon with oriented layers.[32−34] The diffraction pattern of GO shows a sharp peak at 2θ = 11.59° that correlates to the (002) diffraction plane with an interplanar spacing of 5.50 Å, as well as a miniature graphitic peak centered at about 2θ = 26°, which confirms the successful oxidation of graphite.[35,36] The increase in interlayer spacing from graphite to GO confirms the expansion of the graphitic stack due to the presence of oxygen functionalities over graphene layers.[37] The successful reduction of GO is confirmed by the disappearance of the GO characteristic diffraction peak at 2θ = 11.59° and the appearance of the broadened (002) diffraction peak centered at about 2θ = 26° for rGO, N-rGO, rGO/Mn_3O_4, and N-rGO/Mn_3O_4.[36,38] The broadening of the peak at about 26° (between 19 and 25°) for rGO, N-rGO, rGO/Mn_3O_4, and N-rGO/Mn_3O_4 may be ascribed to the presence of disordered rGO layers.[39] Figure 2b illustrates the XRD spectra of N-rGO/Mn_3O_4, rGO/Mn_3O_4, and Mn_3O_4 overlaid with the standard diffraction spectra of the graphitic material (RRUFF ID: R090047) and hausmannite Mn_3O_4 (RRUFF ID: R110179). The peaks from the Mn_3O_4 spectrum can also be observed in the spectra of the nanohybrids, all of which correspond to the diffraction pattern of the hausmannite Mn_3O_4 standard. These peaks, observed at 14.19, 17.94, 28.95, 32.32, 36.05, 38.14, 44.30, 50.79, 58.40, 59.84, and 64.57°, are characteristic of the (001), (101), (112), (103), (211), (004), (220), (105), (321), (224), and (400) diffraction planes of body-centered tetragonal hausmannite Mn_3O_4, respectively.[40] The planes show interlayer spacing values of 6.20, 4.92, 3.09, 2.77, 2.49, 2.36, 2.04, 1.79, 1.58, 1.54, and 1.44 Å, respectively. On average, the interlayer spacing of the samples is calculated at 3.37, 5.50, 3.52, and 5.53 for graphite, GO, rGO, and N-rGO in Figure 2a and at 2.81, 2.80, and 2.75 Å for N-rGO/Mn_3O_4, rGO/Mn_3O_4, and Mn_3O_4 in Figure 2b, respectively. This shows the variation in the interlayer spacing due to the respective treatments used during material preparation. The average in-plane crystallite size of the samples is observed to have decreased from graphite (29.36 nm) to 8.53, 5.15, and 5.57 nm for GO, rGO, and N-rGO, respectively, which is similar to the trends observed in the literature.[37,41] Conversely, the average crystallite sizes of the rGO/Mn_3O_4 and N-rGO/Mn_3O_4 nanohybrids of 12.44 and 15.16 nm, respectively, show a significant decrease with respect to the 24.64 nm for Mn_3O_4, whereas they show a significant increase with respect to the other carbonaceous precursor material.

The Raman spectra in Figure 2c show characteristic D-mode and G-mode bands at 1349 and 1600 cm^{-1}, respectively, for both rGO/Mn_3O_4 and N-rGO/Mn_3O_4 nanohybrids, indicating the defected carbon backbone. The D and G band ratios (I_D/I_G) of the nanohybrids are 1.68 and 1.75, respectively, which did not change significantly from the 1.79, 1.52, and 1.45 of GO, rGO, and N-rGO, respectively. A slight increase in the

https://doi.org/10.1021/acsomega.1c02302
ACS Omega 2021, 6, 31421−31434

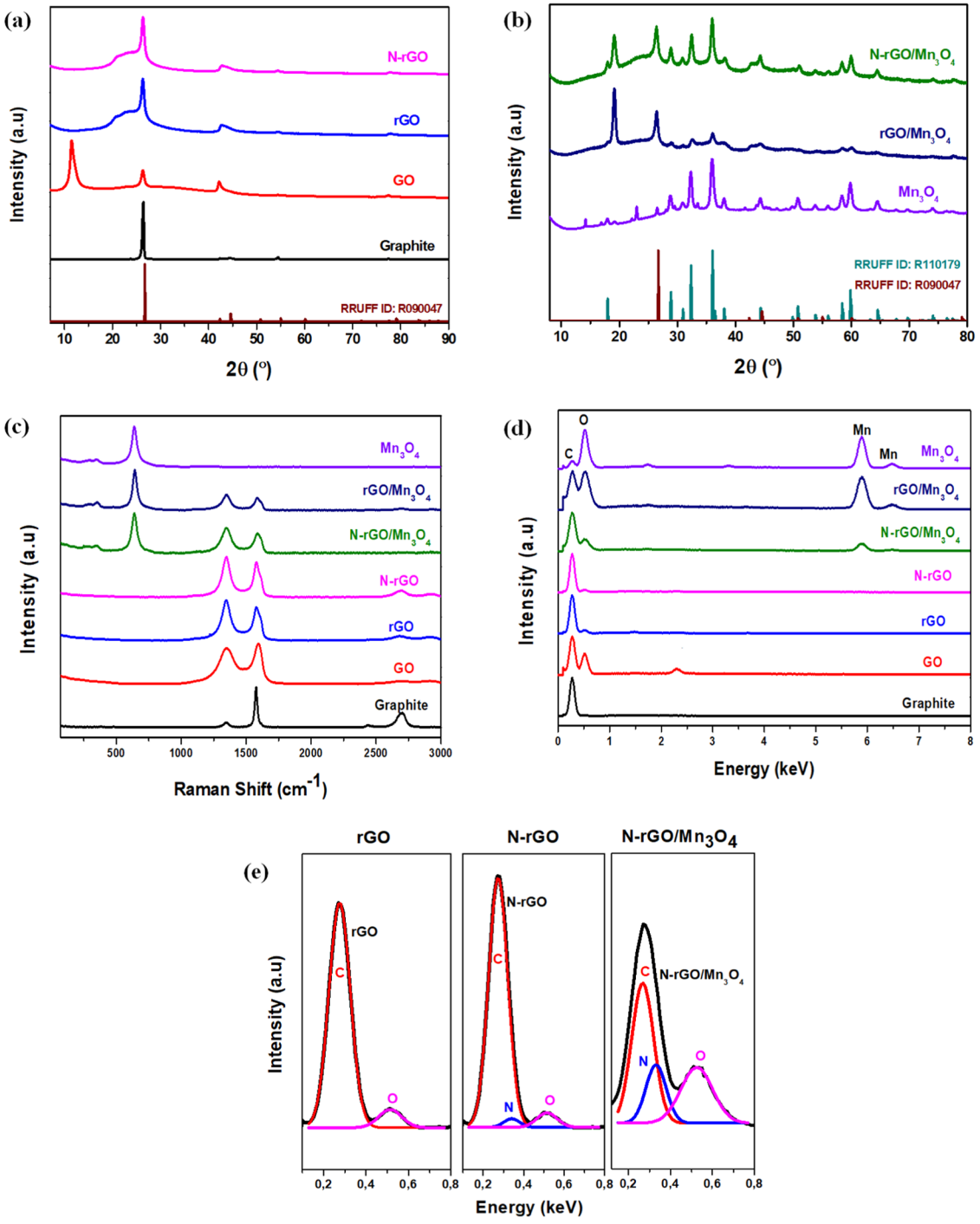

Figure 2. (a) XRD profiles of graphite, GO, rGO, and N-rGO. (b) XRD profiles of N-rGO/Mn_3O_4, rGO/Mn_3O_4, and Mn_3O_4. Raman (c) and EDX (d) spectra of graphite, GO, rGO, N-rGO, N-rGO/Mn_3O_4, rGO/Mn_3O_4, and Mn_3O_4, and (e) deconvoluted EDX spectra of rGO, N-rGO, and N-rGO/Mn_3O_4.

ratio was observed from rGO/Mn_3O_4 to N-rGO/Mn_3O_4, which could be attributed to the increase in the defects brought on by doping nitrogen, added to the growth of hausmannite manganese oxide onto the conjugated carbon framework.[26,42] The presence of crystalline Mn_3O_4 nanoparticles in the nanohybrids is confirmed by the dominant peak at 640 cm^{-1} and the small peaks between 250 and 400 cm^{-1}, which are also seen on the overlaid Mn_3O_4 spectrum.[43,44] The N-rGO/Mn_3O_4 and rGO/Mn_3O_4 nanocomposites are seen to have retained the structural integrity of both rGO and Mn_3O_4.[30] The XRD and Raman results further affirm the SEM image results of the successful integration of Mn_3O_4 with rGO and N-rGO, respectively.

Figure 2d shows the EDX spectra of graphite, GO, rGO, N-rGO, N-rGO/Mn_3O_4, rGO/Mn_3O_4, and Mn_3O_4. A dominant peak characteristic of carbon is observed at 0.25 keV in the EDX spectra, which is due to the carbon coating used and the carbon of the graphitic materials synthesized. An oxygen peak is observed at about 0.52 keV in the spectra of GO, rGO, N-rGO, N-rGO/Mn_3O_4, rGO/Mn_3O_4, and Mn_3O_4, signaling the

https://doi.org/10.1021/acsomega.1c02302
ACS Omega 2021, 6, 31421−31434

presence of oxygen in the samples. A small peak signaling the presence of sulfur in the spectrum of GO comes from using sulfuric acid in the synthesis of GO using the modified Hummers method and is washed away by succeeding procedures. The peaks characteristic of manganese are observed at 5.8 and 6.4 keV in the spectra of N-rGO/Mn_3O_4, rGO/Mn_3O_4, and Mn_3O_4. The miniaturized intensities of the peaks of oxygen and manganese in the spectra of N-rGO/Mn_3O_4 are possibly due to the use of a lot of the carbon coating, which adds to the intensity of the graphene carbon. The presence of nitrogen was confirmed by comparing the deconvoluted spectra of N-rGO and N-rGO/Mn_3O_4 with that of rGO in Figure 2e. A peak of nitrogen can be observed at 0.3 keV in the spectra of N-rGO and N-rGO/Mn_3O_4, which is eclipsed by the peak of carbon. This particular peak is absent in the spectrum of rGO. The successful integration of hausmannite Mn_3O_4 onto N-rGO is further supported by Figure 3, which shows the EDX elemental mapping results for

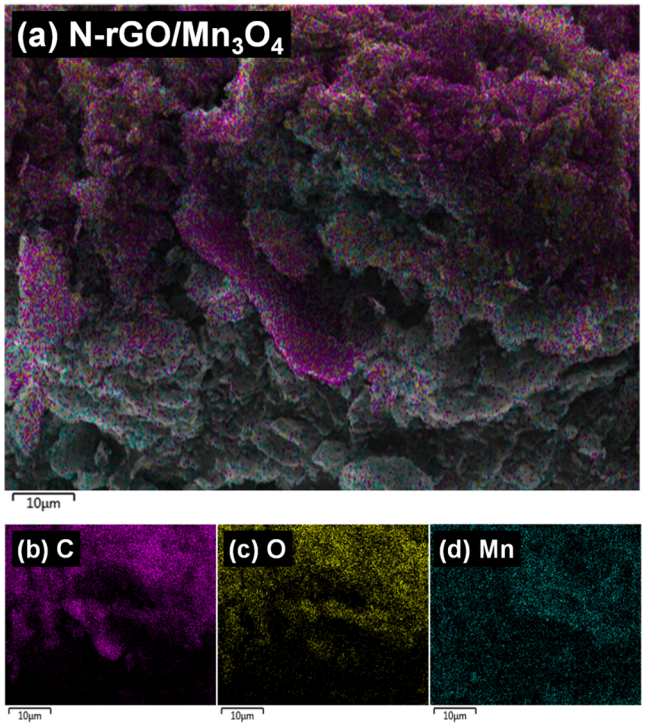

Figure 3. (a) SEM micrograph of N-rGO/Mn_3O_4, and the EDX color mapping for (b) carbon, (c) oxygen, and (d) manganese.

the N-rGO/Mn_3O_4 composite. The images reveal the homogeneous distribution of manganese, carbon, and oxygen throughout the N-rGO sheet, confirming the formation of the N-rGO/metal oxides composite.

3.4. XPS Analysis. X-ray photoelectron spectroscopy (XPS) was used to probe the chemical binding state of the N-rGO/Mn_3O_4 nanohybrid. Figure 4a shows the survey spectra of N-rGO/Mn_3O_4, with peaks indicating the presence of C 1s, O 1s, N 1s, and Mn 2p and the minor Mn 3s and Mn3p peaks. The deconvoluted C 1s spectrum is demonstrated in Figure 4b, with five distinguishable peaks at 284.2, 285, 285.9, 287.9, and 291.3 eV. The major peak at 284.2 eV is characteristic of the graphitic sp^2 carbon, which is a validation of the presence of the graphene backbone. The presence of the sp^2 and sp^3 bonds for the tetrahedral and trigonal phases is demonstrated by the peaks observed at 285 and 285.9 eV, respectively.[45,46] The peak at 287.9 eV is characteristic of the presence of C═O groups.[47] Figure 4c shows three N peaks, which were obtained after deconvolution of the narrow spectrum of N 1s. The three peaks can be attributed to the presence of pyridinic N (397.8 eV), pyrrolic N (400.5 eV), and quaternary N (401.1 eV).[48] As shown in the literature, the presence of the pyridinic and pyrrolic nitrogen in the core structure of graphene improves its electrical and electrochemical performance during the electrochemical process.[49] The narrow oxygen peak (O 1s) was deconvoluted into four peaks, as observed in Figure 4d. The peak observed at 529.8 eV is typical of the bonding configuration of O−Mn atoms in hausmannite Mn_3O_4, while the peak at 531 eV demonstrates the presence of the C═O functional group, and the peak at 532.9 eV reveals the presence of C−O−C/C−OH bonding configurations in rGO.[50,51] As previously reported,[52,53] the peak observed at 530.8 eV is attributed to the formation of a Mn−O−C bond. It was shown that Mn_3O_4 binds with graphene through a bond formed between the manganese ion and oxygen-containing functional groups on the surface of graphene. Formation of the Mn−O−C bond further reduces the oxygen-containing functional groups on rGO by substitution of manganese on C═O and C−OH/C−O−C groups. Figure 4f demonstrates two peaks of Mn 2p at 641.3 and 653.1 eV, which are characteristic of Mn $2p_{3/2}$ and Mn $2p_{1/2}$, respectively. The Mn 2p spectrum shows a splitting width of 11.8 eV, which is a validation that the prominent manganese oxide in the nanohybrid is the Mn_3O_4.[50]

3.5. Electrochemical Evaluations. *3.5.1. Performance of the N-rGO/Mn_3O_4 Nanohybrid in a Symmetric Configuration.* Figure 5a illustrates the cyclic voltammograms of N-rGO/Mn_3O_4, rGO/Mn_3O_4, rGO, N-rGO, and Mn_3O_4 at a scan rate of 5 mV s^{-1}. The cyclic voltammograms of the N-rGO/Mn_3O_4 and rGO/Mn_3O_4 nanohybrids exhibited a quasi-rectangular shape due to the Faradaic charge and pseudocapacitive storage mechanisms of the carbon material and metal oxide, respectively, in the nanohybrid electrode materials. Greater response in current and charge separation was observed from the cyclic voltammograms of the N-rGO/Mn_3O_4 nanohybrid, compared to the rGO/Mn_3O_4 nanohybrid and the precursor materials. The integration of Mn_3O_4 and N-rGO resulted in a synergistic effect on the N-rGO/Mn_3O_4 nanohybrid, enhancing its electrochemical performance as compared to the other synthesized electrode materials in this study. Furthermore, the results show the enhanced electrochemical performance arising from doping nitrogen on the nanohybrid. Figure 5b shows the cyclic voltammograms of N-rGO/Mn_3O_4 at various scan rates ranging from 2 to 100 mV s^{-1} in a potential window range of 0−1.0 V. As in Figure 5a, the cyclic voltammograms illustrated in Figure 5b show the ideal quasi-rectangular shape. The deviation from the perfect rectangular shapes arises from the electrode material's internal resistance that impedes charge mobility within its porous structure.[54] This is demonstrated by the steady change of the curves to a sharp climax that is observed when they approach 1.0 V and the scan rate decreases.

Figure 5c compares the GCD curves of N-rGO/Mn_3O_4, rGO/Mn_3O_4, N-rGO, rGO, and Mn_3O_4 in an aqueous 1 M Na_2SO_4 solution at a current density of 0.1 A/g and a cell voltage range of 0−1.0 V. The fairly symmetrical curves of N-rGO/Mn_3O_4 and rGO/Mn_3O_4 showed excellent capacitive performance and electrochemical reversibility, with N-rGO/

https://doi.org/10.1021/acsomega.1c02302
ACS Omega 2021, 6, 31421−31434

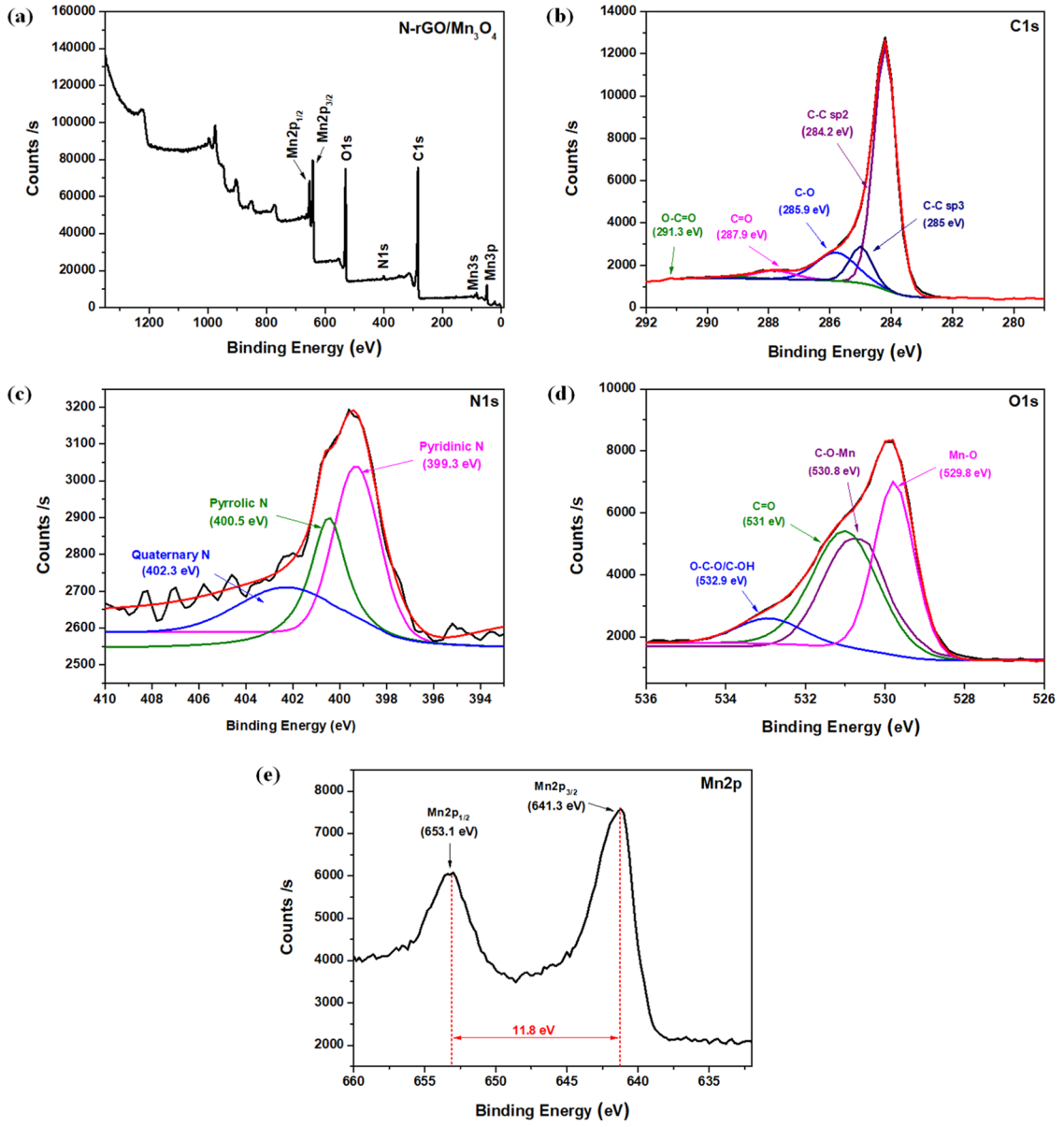

Figure 4. XPS survey spectra of (a) N-rGO/Mn_3O_4, and a narrow spectra of (b) C 1s, (c) N 1s, (d) O 1s, and (e) Mn 2p.

Mn_3O_4 showing superior performance that compliments the CV results. Similar outcomes can be seen in Figure 5d, which illustrates an extensive GCD investigation of N-rGO/Mn_3O_4 at various current densities ranging between 0.1 and 10.0 A g^{-1}. The nanohybrid material showed excellent electrochemical activity at 0.1 A g^{-1}, but it decreased as the current density increased to 10.0 A g^{-1}. This correlates to a decrease in the specific capacitance as current density increases, as shown in Figure 6a, which shows the dependence of C_{sp} on current density for N-rGO/Mn_3O_4, rGO/Mn_3O_4, N-rGO, rGO, and Mn_3O_4. Table 1 demonstrates the inverse relationship of current density with capacitance and energy density and its directly proportional relationship with power density. Using the GCD data obtained from Figure 5c,d and eqs 1−4, the N-rGO/Mn_3O_4 nanohybrid electrode material was found to possess a maximum specific capacitance (C_{sp}) of 345 F g^{-1} and a specific energy density (E_{sp}) of 12.0 Wh kg^{-1} at 0.1 A g^{-1}, which is higher than those for rGO/Mn_3O_4 at 268 F g^{-1} and 9.2 Wh kg^{-1}, respectively. The improved specific capacitance of N-rGO/Mn_3O_4 is attributed to the introduction of the heteroatom (N-doping), which induces surface defects and thus decreases the charge transfer resistance through better accessibility of the electrolyte to the active material.[27] However, the rGO/Mn_3O_4 nanohybrid showed a slightly higher maximum specific power density (P_{max}) of 23.6 kW kg^{-1} at 10.0 A g^{-1} compared to the N-rGO/Mn_3O_4 nanohybrid (22.5 kW kg^{-1}). The Ragone plot in Figure 6b illustrates the specific energy and power densities of N-rGO/Mn_3O_4, rGO/Mn_3O_4, N-rGO, rGO, and Mn_3O_4 at varying current densities (0.1, 0.3, 0.5, 1.0, 2.0, 5.0, and 10.0 A g^{-1}). In comparison to the literature on Mn_3O_4-based aqueous ECs (Table 2), the proficient maximum specific capacitance and higher power-output results of the N-rGO/Mn_3O_4 and rGO/Mn_3O_4 nanohybrid electrode materials put them at an advantage of finding application in systems requiring high energy and power outputs. The N-rGO/Mn_3O_4 nanohybrid electrode has demonstrated the effect of doping nitrogen onto the carbon support (rGO), the synergistic benefit of integrating N-rGO

https://doi.org/10.1021/acsomega.1c02302
ACS Omega 2021, 6, 31421−31434

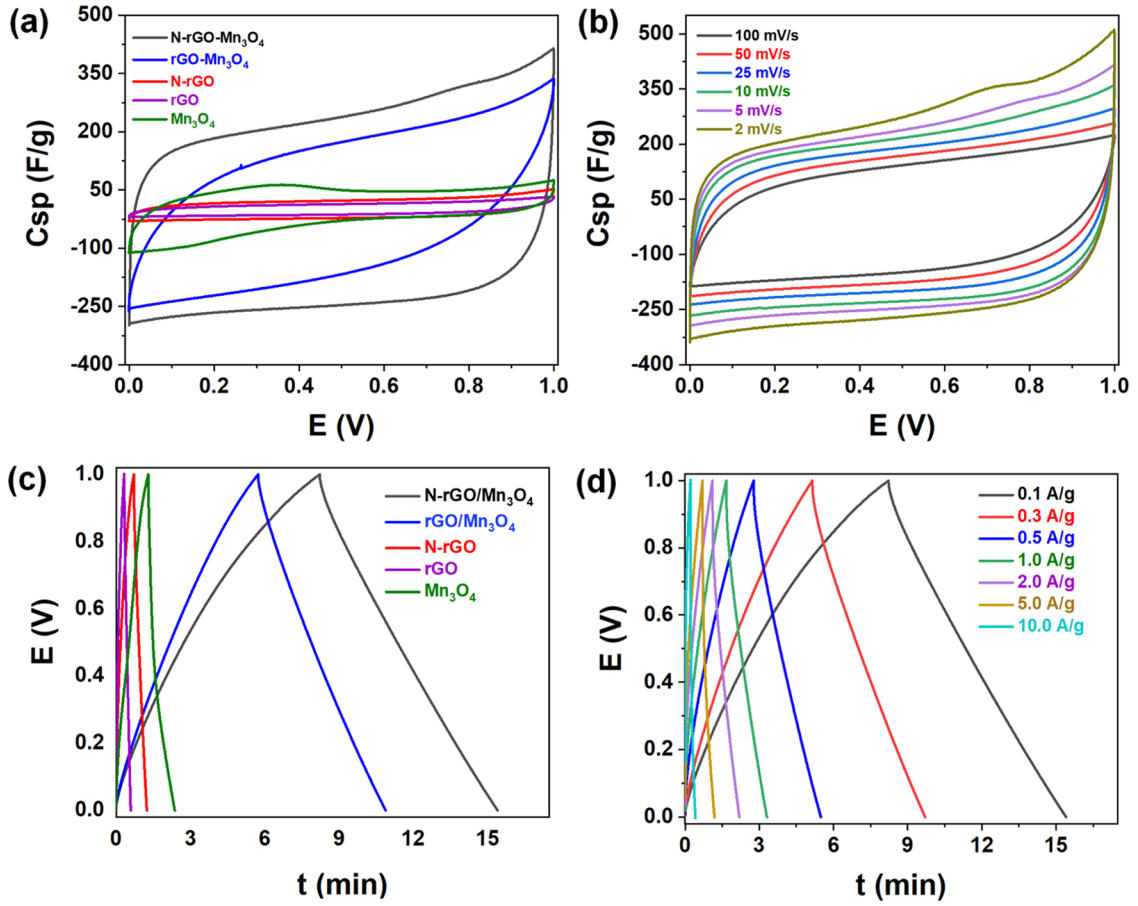

Figure 5. (a) Cyclic voltammograms of N-rGO/Mn_3O_4, rGO/Mn_3O_4, N-rGO, rGO, and Mn_3O_4 at a scan rate of 5 mV/s. (b) Cyclic voltammograms for N-rGO/Mn_3O_4 at various scan rates. (c) Galvanostatic charge−discharge (GCD) curves of N-rGO/Mn_3O_4 and rGO/Mn_3O_4 nanohybrids, N-rGO, rGO, and Mn_3O_4 at a current density of 0.1 A/g. (d) Galvanostatic charge−discharge (GCD) curves of N-rGO/Mn_3O_4 at various current densities in aqueous 1.0 M Na_2SO_4.

and Mn_3O_4, and its competence as electrode material in an symmetric capacitive system (Table 3).

EIS was employed as a valuable technique for better understanding the impedance properties of the synthesized electrode materials in terms of their resistivity and capacitive behaviors. Figure 6c shows the Nyquist plots comparing N-rGO/Mn_3O_4, rGO/Mn_3O_4, N-rGO, rGO, and Mn_3O_4 in a frequency range from 0.1 Hz to 100 kHz with an open-circuit potential. Extrapolating the vertical portion of the Nyquist plot to the real axis of each curve gives the equivalent distributed resistance, which is comprised of both the ionic resistance within the porous electrode material (i.e., the RC semicircle) and the equivalent series resistance (ESR). The resistance from the bulk solution (ESR), which is due to the electrolyte solution, is the x-intercept (i.e., the beginning of the semicircle). The N-rGO/Mn_3O_4 and rGO/Mn_3O_4 nanohybrids showed ESR values of 0.53 and 0.68, respectively, while N-rGO, rGO, and Mn_3O_4 electrode materials displayed the ESR values of 0.35, 0.36, and 0.90 Ω, respectively. The charge transfer resistance (R_{ct}) values for N-rGO (0.45 Ω) and rGO (0.52 Ω) were found to be much smaller than that of the Mn_3O_4 (4.35 Ω). This indicates good charge transfer mobility within the electronic structure of these carbon materials with the ions in the solution as compared to Mn_3O_4. The N-rGO/Mn_3O_4 (1.89 Ω) and rGO/Mn_3O_4 (2.10 Ω) nanohybrids also displayed smaller charge transfer resistance compared to the Mn_3O_4, indicating improved charge mobility due to the synergistic effect between the N-rGO and/or rGO with the Mn_3O_4. The improved electronic properties of N-rGO are induced by the N-doping as compared to the rGO, and a similar trend is witnessed between the N-rGO/Mn_3O_4 in relation to the rGO/Mn_3O_4 nanocomposite. This observation justifies the notion of enhancing the electrochemical properties of the electrode material by doping nitrogen into the structure of the carbon support. This is supported by previous work conducted on nitrogen-doped carbon materials, indicating lower resistance observed from such electrode materials.[60−63] In principle, adequate nitrogen-doping surface modification enhances the wetting of the electrode by the electrolyte,[64−66] thus minimizing the interfacial charge transfer resistance.[67]

The electrochemical stability of the N-rGO/Mn_3O_4 nanohybrid was probed using voltage holding, GCD, and EIS techniques. Figure 7a illustrates the comparative GCD curves after repetitive floating five times for 10 h each interval, and Figure 7b shows the continuous GCD curve after voltage floating for 20 h at a current density of 2.0 A g^{-1}. The nanohybrid electrode material demonstrated outstanding electrochemical stability when cycled under voltage holding for over 50 h, with over 95% capacitance retention, as observed in Figure 7c, which shows the capacitance retention over time. Figure 7d shows the Nyquist plots of before and after voltage holding, while the inset shows a closeup view of the high-frequency region of the two plots.

https://doi.org/10.1021/acsomega.1c02302
ACS Omega 2021, 6, 31421−31434

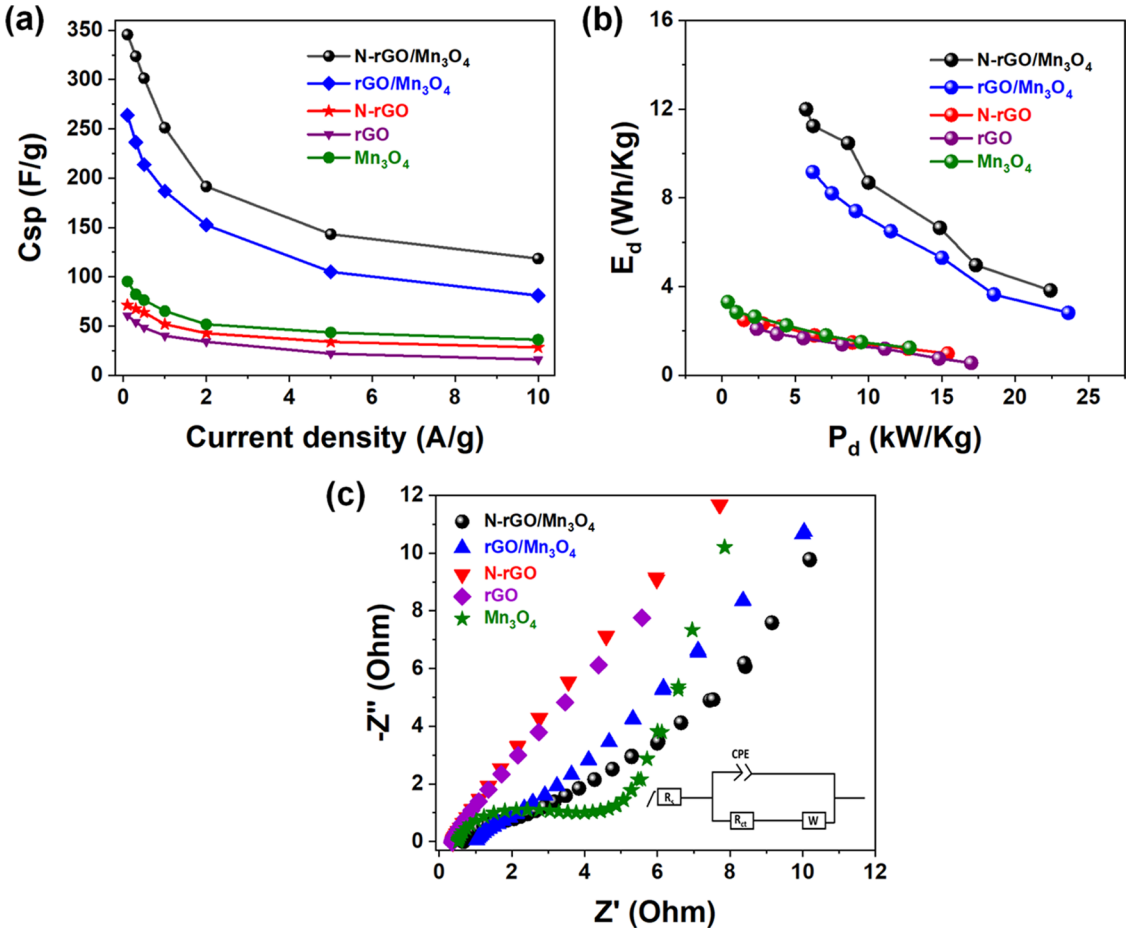

Figure 6. (a) C_{sp} vs current density and (b) Ragone plot (at various current densities: 0.1−10.0 A/g). (c) Nyquist plots of N-rGO/Mn_3O_4, rGO/Mn_3O_4, N-rGO, rGO, and Mn_3O_4. Inset in (c): Randles equivalent circuit used to fit the data; R_s, R_{ct}, CPE, and Z_w are electrolyte resistance, charge transfer resistance, pseudocapacitance, and Warburg impedance, respectively.

Table 1. Comparison of the Electrochemical Performance of the Synthesized Nanohybrids and Their Precursors as Electrode Materials for SC Applications

	C_{sp} (F g^{-1})		E_d (Wh kg^{-1})		P_d (kW kg^{-1})	
	0.1 A g^{-1}	10.0 A g^{-1}	0.1 A g^{-1}	10.0 A g^{-1}	0.1 A g^{-1}	10.0 A g^{-1}
N-rGO/Mn_3O_4	345	123	12	3.8	6.47	22.5
rGO/Mn_3O_4	268	83	9.2	2.9	6.32	23.6
N-rGO	70	28	2.5	1.0	1.96	15.4
rGO	60	18	2.0	0.4	2.5	17.0
Mn_3O_4	95	38	3.3	1.3	0.54	12.9

Table 2. Comparison of the Electrochemical Performance of Mn_3O_4-based Aqueous Symmetric Electrochemical Capacitors from the Literature

electrode	electrolyte	V_{max} (V)	C_{sp} (F g^{-1})	E_{sp} (Wh kg^{-1})	P_{max} (kW kg^{-1})	refs
N-rGO/Mn_3O_4	1.0 M Na_2SO_4	1.0	345	12	22.5	this work
rGO/Mn_3O_4	1.0 M Na_2SO_4	1.0	268	9.2	23.6	this work
N-rGO/Mn_3O_4	1.0 M Na_2SO_4	1.0		2		5
Mn_3O_4@ODC	1.0 M NaOH	1.0	130	4.7		55
HNCXs/Mn_3O_4	1.0 M Li_2SO_4 1 M Li_2SO_4	1.8	248	27.8	4.5	56
Mn_3O_4/PANi/graphene	1.0 M Na_2SO_4	1.0	1240	29.4	0.9	57
NPCM/Mn_3O_4	1.0 M Na_2SO_4	1.6	384	16.5	0.2074	58
Mn_3O_4/MnS	2.0 M KOH	0.6	744			59

3.5.2. Performance of the N-rGO/Mn_3O_4 Nanohybrid in an Asymmetric Configuration. An asymmetric pseudocapacitive system was set up to probe the N-rGO/Mn_3O_4 nanohybrid electrode material's energy density. While the high power density (and hence the fast charge−discharge rate) primarily influences the performance of SCs, improving the

https://doi.org/10.1021/acsomega.1c02302
ACS Omega 2021, 6, 31421−31434

Table 3. Comparison of the Electrochemical Performance of Some Mn_3O_4-based Aqueous Asymmetric Electrochemical Capacitors[a]

electrode	electrolyte	V_{max} (V)	C_{sp} (F g^{-1})	E_{sp} (Wh kg^{-1})	P_{max} (kW kg^{-1})	refs
N-rGO/Mn_3O_4	1.0 M Na_2SO_4	2.0		34.6	14.01	this work
HNCXs/Mn_3O_4	1.0 M Li_2SO_4	2.2	54.5	44.5	5.6	56
NiCo-LDH/Mn_3O_4	KOH/PVA	1.7		57.03	9.7	68
Mn_3O_4@NPC	PVA-Na_2SO_4	2.6		76.96	1.30	69
Mn_3O_4 TB/NHPC	1.0 M Na_2SO_4	1.8	78.3	34.7	7.8	70
Mn_3O_4/rGO	1.0 M Na_2SO_4	0.5	351	36.76	10.0	71
CNT/Mn_3O_4	1.0 M Na_2SO_4	1.8	135.2	37.0	10.3	72
Mn_3O_4@$NiCo_2O_4$@NiO	PVA/KOH	1.6	216	76.8	0.80	73
AC/polyaniline/Mn_3O_4	6 M KOH	1.2		33.8	6.1	74
Mn_3O_4-rGO	1 M Na_2SO_4			31.9	0.50	75
MnO_2/Mn_3O_4	1 M Na_2SO_4	1.6	198.6	234		76
Ti_3C_2-Mn_3O_4	6 M KOH	1.5	78.9**	28.3	2.29	77
Mn_3O_4/Ni$(OH)_2$	1 M KOH	1.6	43	15.3	3.2	78
Mn_3O_4/PCM	3 M KOH	1.4	110.8	27.13	4.67	79

[a]Key: Specific gravimetric capacity (*C g^{-1}, **mAh g^{-1}).

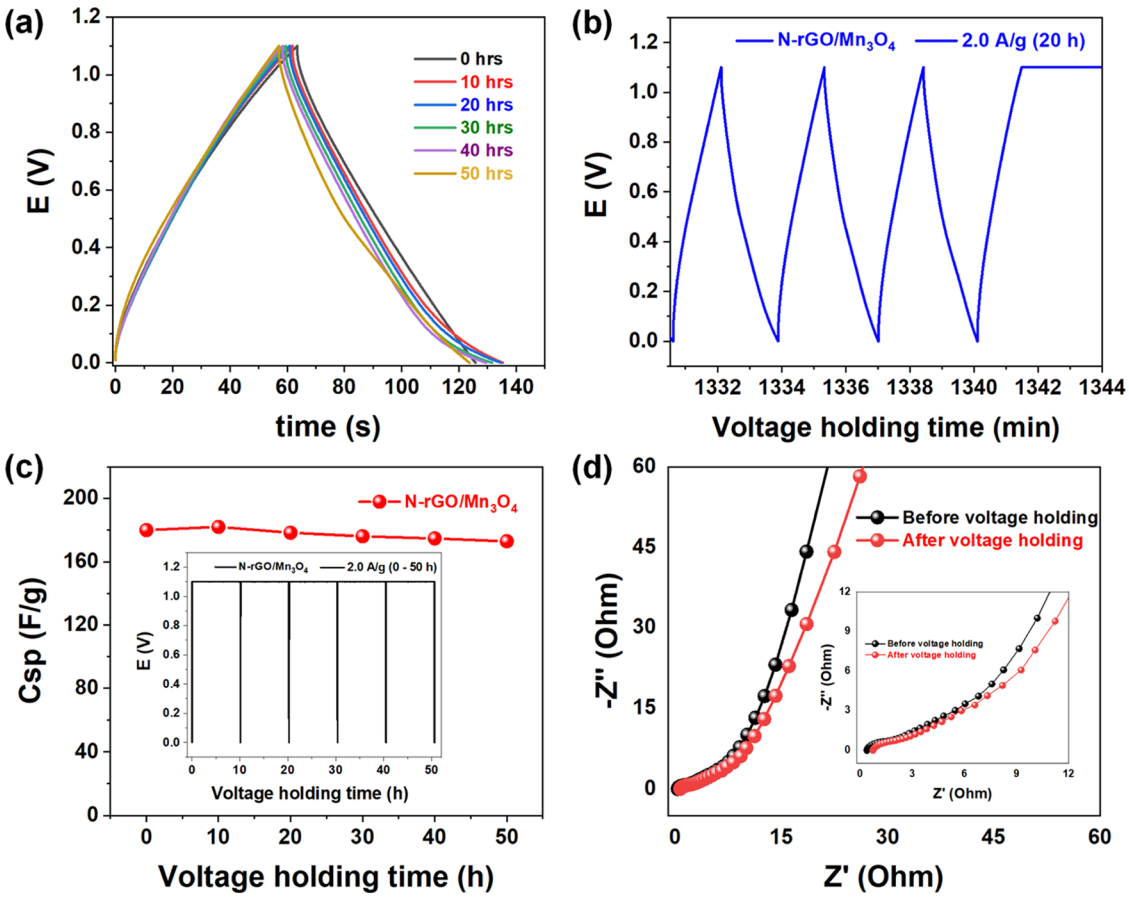

Figure 7. (a) GCD curves at various voltage holding times (0−50 h). (b) Continuous GCD curves after voltage holding for 20 h. (c) Capacitance retention of the electrode material at a current density of 2.0 A g^{-1}, and (d) Nyquist plot (before and after voltage holding) of N-rGO/Mn_3O_4 in aqueous 1.0 M Na_2SO_4 (Inset: closeup view of the high-frequency region).

energy density of SCs is of great significance as it puts it at an advantage to be comparable to LIB application. This aspect can help curb the lag of conventional capacitors to batteries. Figure 8a compares the CV curves of AC (between −1.0 and 0 V vs Ag/AgCl) and that of the N-rGO/Mn_3O_4 nanohybrid (0−1.0 V vs Ag/AgCl) at a scan rate of 5 mV s^{-1} in aqueous 1 M Na_2SO_4. Both curves show acceptable electrochemical stability from which an asymmetric capacitive system capable of reaching a cell voltage of up to 2.0 V in an aqueous electrolyte can be devised. Figure 8b shows cyclic voltammograms of the asymmetric system at varying potential windows (1.4, 1.8, and 2.0 V) of the N-rGO/Mn_3O_4 nanohybrid asymmetric device at a scan rate of 5 mV s^{-1} in 1 M Na_2SO_4. The CV curves demonstrated the ideal quasi-rectangular shape, which suggests impressive electrochemical activity even at the 2.0 V cell potential. Figure 8c depicts the GCD curves of the

https://doi.org/10.1021/acsomega.1c02302
ACS Omega 2021, 6, 31421−31434

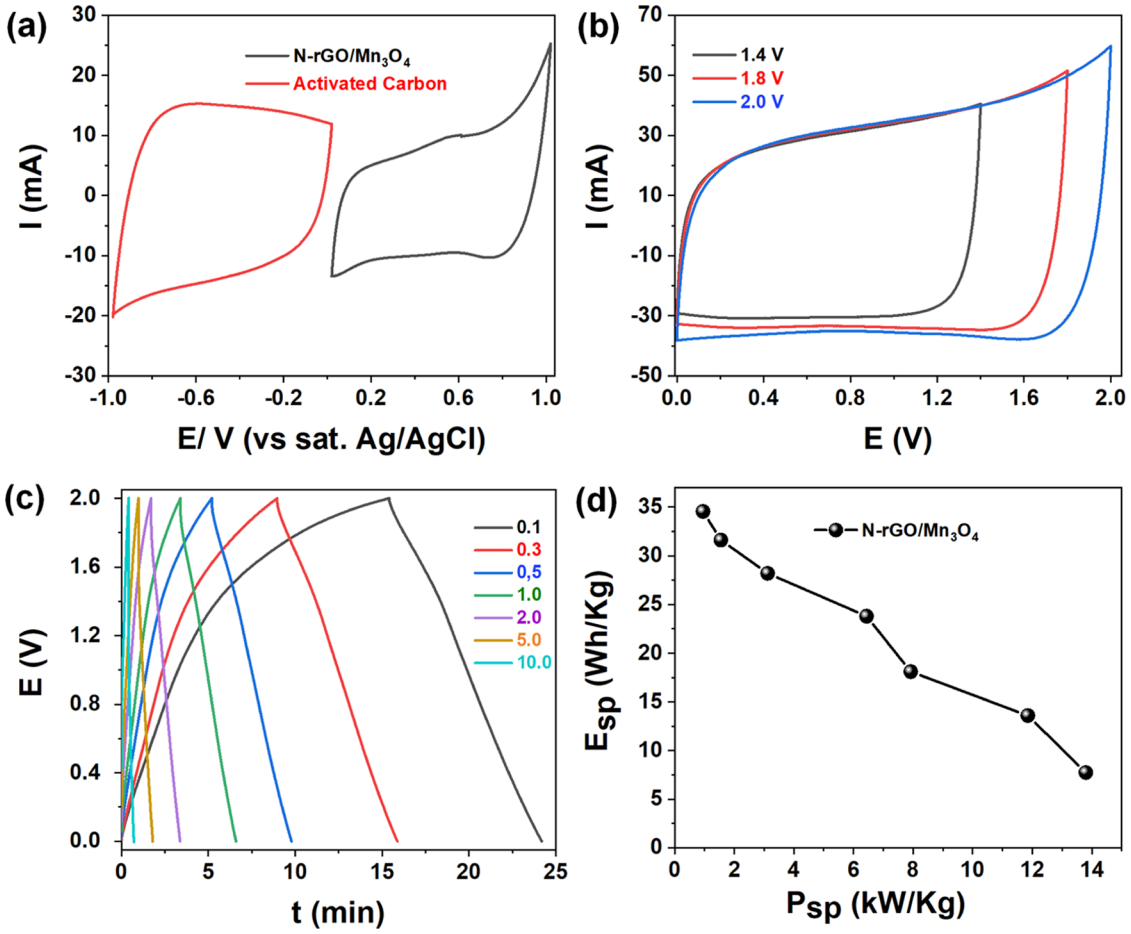

Figure 8. (a) Cyclic voltammograms for the N-rGO/Mn_3O_4 nanohybrid and AC at 5 mV s^{-1}. (b) CV curves at various potential windows (1.4, 1.8, and 2.0 V). (c) GCD curves at various current densities (from 0.1 to 10.0 A/g). (d) Ragone plots at different current densities for N-rGO/Mn_3O_4.

asymmetric system at current densities ranging from 0.1 to 10 A g^{-1}. The asymmetric device showed excellent charge and discharge symmetry, indicating the enhanced electrochemical reversibility and capacitive performance of the system even at a maximum high cell potential of 2.0 V. The Ragone plot shown in Figure 8d demonstrates the asymmetric device as possessing an excellent maximum energy density of *ca.* 34.6 Wh kg^{-1} at a current density of 0.1 A g^{-1} and a maximum power density of 14.01 kW kg^{-1} at 10 A g^{-1}. These outstanding results are observed to be comparable to previously reported literature on asymmetric ECs, as outlined in Table 2.

4. CONCLUSIONS

This study sought to investigate the electrochemical performance of the one-step synthesized nitrogen-doped reduced graphene oxide/hausmannite manganese oxide (N-rGO/Mn_3O_4) nanohybrid, its application as a pseudocapacitor electrode material in symmetric and asymmetric devices, and the effects of doping nitrogen on the reduced graphene oxide (rGO)-based carbon support. The N-rGO/Mn_3O_4 and rGO/Mn_3O_4 nanohybrids showed exceptional pseudocapacitive behavior in relation to the individual precursor materials (i.e., rGO, N-rGO, and Mn_3O_4). The N-rGO/Mn_3O_4 electrode material demonstrated a high specific capacitance of 345 F g^{-1} at a current density of 0.1 A g^{-1}, excellent specific energy (12.0 Wh kg^{-1}), high power density (22.5 kW kg^{-1}), and excellent cycle stability in a symmetrical pseudocapacitive setup (see Figure 6), while the rGO/Mn_3O_4 nanohybrid displayed a high specific capacitance of 264 F g (0.1 A g^{-1}) with excellent specific energy and power densities of 9.2 Wh kg^{-1} and 23.6 kW kg^{-1}, respectively. The N-rGO/Mn_3O_4 nanohybrid electrode material also displayed an impressive asymmetric pseudocapacitive performance with a stable potential window of 2.0 V in 1.0 M Na_2SO_4 electrolyte, a maximum energy density of 34.6 Wh kg^{-1}, and a maximum power density of 14.01 kW kg^{-1}. From the results obtained, this study has rationally demonstrated the excellent electrochemical performance and capacitive behavior of the N-rGO/Mn_3O_4 and rGO/Mn_3O_4 nanohybrids, which can be attributed to the synergistic effect of integrating N-rGO/ rGO on Mn_3O_4.

AUTHOR INFORMATION

Corresponding Authors

Katlego Makgopa − *Department of Chemistry, Faculty of Science, Tshwane University of Technology (Arcadia Campus), Pretoria 0001, South Africa;* orcid.org/0000-0003-2750-9790; Email: MakgopaK@tut.ac.za

Kwena D. Modibane − *Department of Chemistry, School of Physical and Mineral Sciences, University of Limpopo (Turfloop Campus), 0727 Polokwane, South Africa;* orcid.org/0000-0003-4502-122X; Email: Kwena.Modibane@ul.ac.za

https://doi.org/10.1021/acsomega.1c02302
ACS Omega 2021, 6, 31421−31434

Authors

Mpho S. Ratsoma − *Department of Chemistry, Faculty of Science, Tshwane University of Technology (Arcadia Campus), Pretoria 0001, South Africa;* orcid.org/0000-0001-7193-938X

Kumar Raju − *Electrochemical Energy Technologies (EET), Energy Centre, Council for Scientific and Industrial Research (CSIR), Pretoria 0001, South Africa;* orcid.org/0000-0002-6143-0720

Letlhogonolo F. Mabena − *Department of Chemistry, Faculty of Science, Tshwane University of Technology (Arcadia Campus), Pretoria 0001, South Africa;* orcid.org/0000-0001-7643-8090

Complete contact information is available at: https://pubs.acs.org/10.1021/acsomega.1c02302

Notes

The authors declare no competing financial interest.

■ ACKNOWLEDGMENTS

K.M., K.D.M., and L.F.M. thank the financial support from the National Research Foundation (NRF) under the Thuthuka programme (UID Nos. 117984, 118113, and 113561). MSR thanks the Gauteng City Region Academy (GCRA) for the postgraduate financial support.

■ REFERENCES

(1) Liu, C.; Li, F.; Lai-Peng, M.; Cheng, H. M. Advanced Materials for Energy Storage. *Adv. Mater.* **2010**, *22*, E28−E62.

(2) Patra, T.; Panda, J.; Sahoo, T. R. Synthesis of Mn3O4nano-particles via Microwave Combustion Route for Electrochemical Energy Storage Application. *Mater. Today Proc.* **2021**, *41*, 247−250.

(3) Rani, B. J.; Ravina, M.; Ravi, G.; Ravichandran, S.; Ganesh, V.; Yuvakkumar, R. Synthesis and Characterization of Hausmannite (Mn3O4) Nanostructures. *Surf. Interfaces* **2018**, *11*, 28−36.

(4) Ponnusamy, P. M.; Agilan, S.; Muthukumarasamy, N.; Senthil, T. S.; Rajesh, G.; Venkatraman, M. R.; Velauthapillai, D. Structural, Optical and Magnetic Properties of Undoped NiO and Fe-Doped NiO Nanoparticles Synthesized by Wet-Chemical Process. *Mater. Charact.* **2016**, *114*, 166−171.

(5) Zhou, X.; Meng, T.; Yi, F.; Shu, D.; Li, Z.; Zeng, Q.; Gao, A.; Zhu, Z. Supramolecular Assisted Fabrication of Mn3O4 Anchored Nitrogen-Doped Reduced Graphene Oxide and Its Distinctive Electrochemical Activation Process during Supercapacitive Study. *Electrochim. Acta* **2021**, *370*, No. 137739.

(6) Miller, J. R.; Simon, P. The Chalkboard: Fundamentals of Electrochemical Capacitor Design and Operation. *Electrochem. Soc. Interface* **2008**, *17*, 31−32.

(7) Yang, L.; Cheng, S.; Wang, J.; Ji, X.; Jiang, Y.; Yao, M.; Wu, P.; Wang, M.; Zhou, J.; Liu, M. Investigation into the Origin of High Stability of δ-MnO2 Pseudo-Capacitive Electrode Using Operando Raman Spectroscopy. *Nano Energy* **2016**, *30*, 293−302.

(8) Jafta, C. J.; Nkosi, F.; le Roux, L.; Mathe, M. K.; Kebede, M.; Makgopa, K.; Song, Y.; Tong, D.; Oyama, M.; Manyala, N.; Chen, S.; Ozoemena, K. I. Manganese Oxide/Graphene Oxide Composites for High-Energy Aqueous Asymmetric Electrochemical Capacitors. *Electrochim. Acta* **2013**, *110*, 228−233.

(9) Chen, T.; Dai, L. Carbon Nanomaterials for High-Performance Supercapacitors. *Mater. Today* **2013**, *16*, 272−280.

(10) Zhang, X.; Tao, L.; He, P.; Zhang, X.; He, M.; Dong, F.; He, S.; Li, C.; Liu, H.; Wang, S.; Zhang, Y. A Novel Cobalt Hexacyanoferrate/Multi-Walled Carbon Nanotubes Nanocomposite: Spontaneous Assembly Synthesis and Application as Electrode Materials with Significantly Improved Capacitance for Super-capacitors. *Electrochim. Acta* **2018**, *259*, 793−802.

(11) Zhang, L. L.; Zhao, X. S. Carbon-Based Materials as Supercapacitor Electrodes. *Chem. Soc. Rev.* **2009**, *38*, No. 2520.

(12) Mirghni, A. A.; Madito, M. J.; Masikhwa, T. M.; Oyedotun, K. O.; Bello, A.; Manyala, N. Hydrothermal Synthesis of Manganese Phosphate/Graphene Foam Composite for Electrochemical Super-capacitor Applications. *J. Colloid Interface Sci.* **2017**, *494*, 325−337.

(13) Makgopa, K.; Mabena, L. F.; Brink, C. G.; Chauke, G. N.; Teffu, M. D.; Modibane, K. D.; Hato, M. J. Nanostructured Carbon-Based Electrode Materials for Supercapacitor Applications. *Carbon Related Materials*; Springer Singapore: Singapore, 2021; pp 317−355.

(14) Wang, G.; Zhang, L.; Zhang, J. A Review of Electrode Materials for Electrochemical Supercapacitors. *Chem. Soc. Rev.* **2012**, *41*, 797−828.

(15) Rorabeck, K.; Zhitomirsky, I. Salting-out Aided Dispersive Extraction of Mn3O4 Nanoparticles and Carbon Nanotubes for Application in Supercapacitors. *Colloids Surfaces A Physicochem. Eng. Asp.* **2021**, *618*, No. 126451.

(16) Wang, Y.; Cheng, L.; Li, F.; Xiong, H.; Xia, Y. High Electrocatalytic Performance of Mn3O4/Mesoporous Carbon Composite for Oxygen Reduction in Alkaline Solutions. *Chem. Mater.* **2007**, *19*, 2095−2101.

(17) Bharath, G.; Arora, N.; Hai, A.; Banat, F.; Savariraj, D.; Taher, H.; Mangalaraja, R. V. Synthesis of Hierarchical Mn3O4 Nanowires on Reduced Graphene Oxide Nanoarchitecture as Effective Pseudocapacitive Electrodes for Capacitive Desalination Application. *Electrochim. Acta* **2020**, *337*, No. 135668.

(18) Makgopa, K.; Ejikeme, P. M.; Jafta, C. J.; Raju, K.; Zeiger, M.; Presser, V.; Ozoemena, K. I. A High-Rate Aqueous Symmetric Pseudocapacitor Based on Highly Graphitized Onion-like Carbon/Birnessite-Type Manganese Oxide Nanohybrids. *J. Mater. Chem. A* **2015**, *3*, 3480−3490.

(19) Makgopa, K.; Raju, K.; Ejikeme, P. M.; Ozoemena, K. I. High-Performance Mn3O4/Onion-like Carbon (OLC) Nanohybrid Pseudocapacitor: Unravelling the Intrinsic Properties of OLC against Other Carbon Supports. *Carbon* **2017**, *117*, 20−32.

(20) Makgopa, K.; Bello, A.; Raju, K.; Modibane, K. D.; Hato, M. J. Nanostructured Metal Oxides for Supercapacitor Applications. In *Environmental Chemistry for a Sustainable World*; 2019; pp 247−303.

(21) Jiang, J.; Kucernak, A. Electrochemical Supercapacitor Material Based on Manganese Oxide: Preparation and Characterization. *Electrochim. Acta* **2002**, *47*, 2381−2386.

(22) An, G.; Yu, P.; Xiao, M.; Liu, Z.; Miao, Z.; Ding, K.; Mao, L. Low-Temperature Synthesis of Mn3O4 Nanoparticles Loaded on Multi-Walled Carbon Nanotubes and Their Application in Electro-chemical Capacitors. *Nanotechnology* **2008**, *19*, No. 275709.

(23) Qiao, Y.; Sun, Q.; Cui, H.; Wang, D.; Yang, F.; Wang, X. Synthesis of Micro/Nano-Structured Mn3O4 for Supercapacitor Electrode with Excellent Rate Performance. *RSC Adv.* **2015**, *5*, 31942−31946.

(24) Susi, T.; Kotakoski, J.; Arenal, R.; Kurasch, S.; Jiang, H.; Skakalova, V.; Stephan, O.; Krasheninnikov, A. V.; Kauppinen, E. I.; Kaiser, U.; Meyer, J. C. Atomistic Description of Electron Beam Damage in Nitrogen-Doped Graphene and Single-Walled Carbon Nanotubes. *ACS Nano* **2012**, *6*, 8837−8846.

(25) Xue, Y.; Liu, J.; Chen, H.; Wang, R.; Li, D.; Qu, J.; Dai, L. Nitrogen-Doped Graphene Foams as Metal-Free Counter Electrodes in High-Performance Dye-Sensitized Solar Cells. *Angew. Chem. Int. Ed.* **2012**, *51*, 12124−12127.

(26) Geng, D.; Yang, S.; Zhang, Y.; Yang, J.; Liu, J.; Li, R.; Sham, T. K.; Sun, X.; Ye, S.; Knights, S. Nitrogen Doping Effects on the Structure of Graphene. *Appl. Surf. Sci.* **2011**, *257*, 9193−9198.

(27) Wang, T.; Wang, L. X.; Wu, D. L.; Xia, W.; Jia, D. Z. Interaction between Nitrogen and Sulfur in Co-Doped Graphene and Synergetic Effect in Supercapacitor. *Sci. Rep.* **2015**, *5*, No. 9591.

(28) Hummers, W. S.; Offeman, R. E. Preparation of Graphitic Oxide. *J. Am. Chem. Soc.* **1958**, *80*, 1339.

(29) Dey, R. S.; Raj, C. R. Development of an Amperometric Cholesterol Biosensor Based on Graphene−Pt Nanoparticle Hybrid Material. *J. Phys. Chem. C* **2010**, *114*, 21427−21433.

(30) Bag, S.; Roy, K.; Gopinath, C. S.; Raj, C. R. Facile Single-Step Synthesis of Nitrogen-Doped Reduced Graphene Oxide-Mn3O4 Hybrid Functional Material for the Electrocatalytic Reduction of Oxygen. *ACS Appl. Mater. Interfaces* **2014**, *6*, 2692−2699.
(31) Béguin, F.; Presser, V.; Balducci, A.; Frackowiak, E. Carbons and Electrolytes for Advanced Supercapacitors. *Adv. Mater.* **2014**, *26*, 2219−2251.
(32) Bacon, G. E. The Interlayer Spacing of Graphite. *Acta Crystallogr.* **1951**, *4*, 558−561.
(33) Franklin, R. E. The Structure of Graphitic Carbons. *Acta Crystallogr.* **1951**, *4*, 253−261.
(34) Franklin, R. E. Crystallite Growth in Graphitizing and Non-Graphitizing Carbons. *Proc. R. Soc. London. Ser. A. Math. Phys. Sci.* **1951**, *209*, 196−218.
(35) Fan, Z. J.; Kai, W.; Yan, J.; Wei, T.; Zhi, L. J.; Feng, J.; Ren, Y. M.; Song, L. P.; Wei, F. Facile Synthesis of Graphene Nanosheets via Fe Reduction of Exfoliated Graphite Oxide. *ACS Nano* **2011**, *5*, 191−198.
(36) Wang, L.; Ding, J.; Chai, Y.; Liu, Q.; Ren, J.; Liu, X.; Dai, W. L. CeO2 Nanorod/g-C3N4/N-RGO Composite: Enhanced Visible-Light-Driven Photocatalytic Performance and the Role of N-RGO as Electronic Transfer Media. *Dalt. Trans.* **2015**, *44*, 11223−11234.
(37) Sharma, R.; Chadha, N.; Saini, P. Determination of Defect Density, Crystallite Size and Number of Graphene Layers in Graphene Analogues Using X-Ray Diffraction and Raman Spectroscopy. *Indian J. Pure Appl. Phys.* **2017**, *55*, 625−629.
(38) Xiong, B.; Zhou, Y.; Zhao, Y.; Wang, J.; Chen, X.; O'Hayre, R.; Shao, Z. The Use of Nitrogen-Doped Graphene Supporting Pt Nanoparticles as a Catalyst for Methanol Electrocatalytic Oxidation. *Carbon* **2013**, *52*, 181−192.
(39) Chen, H.; Müller, M. B.; Gilmore, K. J.; Wallace, G. G.; Li, D. Mechanically Strong, Electrically Conductive, and Biocompatible Graphene Paper. *Adv. Mater.* **2008**, *20*, 3557−3561.
(40) Nagamuthu, S.; Vijayakumar, S.; Muralidharan, G. Synthesis of Mn3O4-Amorphous Carbon Nanoparticles as ElectrodeMaterial for High Performance Supercapacitor Applications. *Energy Fuels* **2013**, *27*, 3508−3515.
(41) Kaushal, A.; Dhawan, S. K.; Singh, V. Determination of Crystallite Size, Number of Graphene Layers and Defect Density of Graphene Oxide (GO) and Reduced Graphene Oxide (RGO), *AIP Conference Proceedings*, 2019; pp 1−5.
(42) Tuinstra, F.; Koenig, J. L. Raman Spectrum of Graphite. *J. Chem. Phys.* **1970**, *53*, 1126−1130.
(43) Lee, J. W.; Hall, A. S.; Kim, J. D.; Mallouk, T. E. A Facile and Template-Free Hydrothermal Synthesis of Mn3O4nanorods on Graphene Sheets for Supercapacitor Electrodes with Long Cycle Stability. *Chem. Mater.* **2012**, *24*, 1158−1164.
(44) Buciuman, F.; Patcas, F.; Craciun, R.; R. T. Zahn, D. Vibrational Spectroscopy of Bulk and Supported Manganese Oxides. *Phys. Chem. Chem. Phys.* **1999**, *1*, 185−190.
(45) Jang, J. W.; Lee, C. E.; Lyu, S. C.; Lee, T. J.; Lee, C. J. Structural Study of Nitrogen-Doping Effects in Bamboo-Shaped Multiwalled Carbon Nanotubes. *Appl. Phys. Lett.* **2004**, *84*, 2877−2879.
(46) Wei, D.; Liu, Y.; Wang, Y.; Zhang, H.; Huang, L.; Yu, G. Synthesis of N-Doped Graphene by Chemical Vapor Deposition and Its Electrical Properties. *Nano Lett.* **2009**, *9*, 1752−1758.
(47) Zhou, J.; Song, H.; Ma, L.; Chen, X. Magnetite/Graphene Nanosheet Composites: Interfacial Interaction and Its Impact on the Durable High-Rate Performance in Lithium-Ion Batteries. *RSC Adv.* **2011**, *1*, 782−791.
(48) Jeong, H. M.; Lee, J. W.; Shin, W. H.; Choi, Y. J.; Shin, H. J.; Kang, J. K.; Choi, J. W. Nitrogen-Doped Graphene for High-Performance Ultracapacitors and the Importance of Nitrogen-Doped Sites at Basal Planes. *Nano Lett.* **2011**, *11*, 2472−2477.
(49) Wu, Z. S.; Ren, W.; Xu, L.; Li, F.; Cheng, H. M. Doped Graphene Sheets as Anode Materials with Superhigh Rate and Large Capacity for Lithium Ion Batteries. *ACS Nano* **2011**, *5*, 5463−5471.
(50) Oku, M.; Hirokawa, K.; Ikeda, S. X-Ray Photoelectron Spectroscopy of Manganese—Oxygen Systems. *J. Electron Spectros. Relat. Phenomena* **1975**, *7*, 465−473.
(51) Hontoria-Lucas, C.; López-Peinado, A. J.; López-González, J. deD.; Rojas-Cervantes, M. L.; Martín-Aranda, R. M. Study of Oxygen-Containing Groups in a Series of Graphite Oxides: Physical and Chemical Characterization. *Carbon* **1995**, *33*, 1585−1592.
(52) Yang, S.; Song, X.; Zhang, P.; Gao, L. Crumpled Nitrogen-Doped Graphene-Ultrafine Mn3O4 Nanohybrids and Their Application in Supercapacitors. *J. Mater. Chem. A* **2013**, *1*, 14162−14169.
(53) Zhou, G.; Wang, D. W.; Yin, L. C.; Li, N.; Li, F.; Cheng, H. M. Oxygen Bridges between Nio Nanosheets and Graphene for Improvement of Lithium Storage. *ACS Nano* **2012**, *6*, 3214−3223.
(54) Wang, B.; Park, J.; Wang, C.; Ahn, H.; Wang, G. Mn3O4 Nanoparticles Embedded into Graphene Nanosheets: Preparation, Characterization, and Electrochemical Properties for Supercapacitors. *Electrochim. Acta* **2010**, *55*, 6812−6817.
(55) Arenas-Esteban, D.; Urones-Garrote, E.; Carretero-González, J.; Birss, V.; Otero-Diáz, L. C.; Ávila-Brande, D. Organometallic-Derived Carbon (ODC)-Metal Nano-Oxide Composites as Improved Electrode Materials for Supercapacitors. *Inorg. Chem.* **2019**, *58*, 9175−9180.
(56) Liu, X.; Zhong, M.; Fu, Z.; Xu, X.; Wang, C.; Yuan, L.; Tang, Y. From Hierarchically Porous Carbon to Mn3O4/Carbon Composites for High Voltage Aqueous Supercapacitors. *J. Power Sources* **2021**, *485*, No. 229111.
(57) Haldar, P.; Biswas, S.; Sharma, V.; Chowdhury, A.; Chandra, A. Mn3O4-Polyaniline-Graphene as Distinctive Composite for Use in High-Performance Supercapacitors. *Appl. Surf. Sci.* **2019**, *491*, 171−179.
(58) Sun, L.; Song, G.; Sun, Y.; Fu, Q.; Pan, C. One-Step Construction of 3D N/P-Codoped Hierarchically Porous Carbon Framework in-Situ Armored Mn3O4 Nanoparticles for High-Performance Flexible Supercapacitors. *Electrochim. Acta* **2020**, *333*, No. 135496.
(59) Wang, Z.; Jia, H.; Cai, Y.; Li, C.; Zheng, X.; Liang, H.; Qi, J.; Cao, J.; Feng, J. Highly Conductive Mn3O4/MnS Heterostructures Building Multi-Shelled Hollow Microspheres for High-Performance Supercapacitors. *Chem. Eng. J.* **2020**, *392*, No. 123890.
(60) Wang, Y.; Wang, J.; Morimoto, S.; Hong Melvin, G. J.; Zhao, R.; Hashimoto, Y.; Terrones, M. Nitrogen-Doped Porous Carbon Monoliths from Molecular-Level Dispersion of Carbon Nanotubes into Polyacrylonitrile (PAN) and the Effect of Carbonization Process for Supercapacitors. *Carbon* **2019**, *143*, 776−785.
(61) Wang, D.-W.; Li, F.; Yin, L.-C.; Lu, X.; Chen, Z.-G.; Gentle, I. R.; Lu, G. Q. Max.; Cheng, H.-M. Nitrogen-Doped Carbon Monolith for Alkaline Supercapacitors and Understanding Nitrogen-Induced Redox Transitions. *Chem. - A Eur. J.* **2012**, *18*, 5345−5351.
(62) Lin, T.; Chen, I.-W.; Liu, F.; Yang, C.; Bi, H.; Xu, F.; Huang, F. Nitrogen-Doped Mesoporous Carbon of Extraordinary Capacitance for Electrochemical Energy Storage. *Science* **2015**, *350*, 1508−1513.
(63) Chen, L.-F.; Zhang, X.-D.; Liang, H.-W.; Kong, M.; Guan, Q.-F.; Chen, P.; Wu, Z.-Y.; Yu, S.-H. Synthesis of Nitrogen-Doped Porous Carbon Nanofibers as an Efficient Electrode Material for Supercapacitors. *ACS Nano* **2012**, *6*, 7092−7102.
(64) Hou, P.-X.; Orikasa, H.; Yamazaki, T.; Matsuoka, K.; Tomita, A.; Setoyama, N.; Fukushima, Y.; Kyotani, T. Synthesis of Nitrogen-Containing Microporous Carbon with a Highly Ordered Structure and Effect of Nitrogen Doping on H2O Adsorption. *Chem. Mater.* **2005**, *17*, 5187−5193.
(65) Horikawa, T.; Sakao, N.; Sekida, T.; Hayashi, J.; Do, D. D.; Katoh, M. Preparation of Nitrogen-Doped Porous Carbon by Ammonia Gas Treatment and the Effects of N-Doping on Water Adsorption. *Carbon* **2012**, *50*, 1833−1842.
(66) Liu, H.; Song, H.; Chen, X.; Zhang, S.; Zhou, J.; Ma, Z. Effects of Nitrogen- and Oxygen-Containing Functional Groups of Activated Carbon Nanotubes on the Electrochemical Performance in Supercapacitors. *J. Power Sources* **2015**, *285*, 303−309.

https://doi.org/10.1021/acsomega.1c02302
ACS Omega 2021, 6, 31421−31434

(67) Sun, L.; Tian, C.; Fu, Y.; Yang, Y.; Yin, J.; Wang, L.; Fu, H. Nitrogen-Doped Porous Graphitic Carbon as an Excellent Electrode Material for Advanced Supercapacitors. *Chem. - A Eur. J.* **2014**, *20*, 564−574.
(68) Zhao, N.; Fan, H.; Zhang, M.; Wang, C.; Ren, X.; Peng, H.; Li, H.; Jiang, X.; Cao, X. Preparation of Partially-Cladding NiCo-LDH/Mn3O4 Composite by Electrodeposition Route and Its Excellent Supercapacitor Performance. *J. Alloys Compd.* **2019**, *796*, 111−119.
(69) Ding, Y.; Dai, L.; Wang, R.; Wang, H.; Zhang, H.; Jiang, W.; Tang, J.; Zang, S.-Q. Bio-Inspired Hierarchical Mn3O4@N, P-Doped Carbon Cathode for High-Performance 2.6V Flexible Aqueous Asymmetric Supercapacitors. *Chem. Eng. J.* **2021**, *407*, No. 126874.
(70) Cheng, Y.; Li, B.; Wei, Z.; Wang, Y.; Wei, D.; Jia, D.; Feng, Y.; Zhou, Y. Mn3O4 Tetragonal Bipyramid Laden Nitrogen Doped and Hierarchically Porous Carbon Composite as Positive Electrode for High-Performance Asymmetric Supercapacitor. *J. Power Sources* **2020**, *451*, No. 227775.
(71) Huang, Z.; Li, S.; Li, Z.; Li, J.; Zhang, G.; Cao, L.; Liu, H. Mn3O4 Nanoflakes/RGO Composites with Moderate Pore Size and (O═)C-O-Mn Bond for Enhanced Supercapacitor Performance. *J. Alloys Compd.* **2020**, *830*, No. 154637.
(72) Kumar, A.; Sarkar, D.; Mukherjee, S.; Patil, S.; Sarma, D. D.; Shukla, A. Realizing an Asymmetric Supercapacitor Employing Carbon Nanotubes Anchored to Mn 3 O 4 Cathode and Fe 3 O 4 Anode. *ACS Appl. Mater. Interfaces* **2018**, *10*, 42484−42493.
(73) Feng, X.; Huang, Y.; Li, C.; Xiao, Y.; Chen, X.; Gao, X.; Chen, C. Construction of Carnations-like Mn3O4@NiCo2O4@NiO Hierarchical Nanostructures for High-Performance Supercapacitors. *Electrochim. Acta* **2019**, *308*, 142−149.
(74) Zhuang, R.; Dong, Y.; Li, D.; Liu, R.; Zhang, S.; Yu, Y.; Song, H.; Ma, J.; Liu, X.; Chen, X. Polyaniline-Mediated Coupling of Mn3O4 Nanoparticles on Activated Carbon for High-Performance Asymmetric Supercapacitors. *J. Alloys Compd.* **2021**, *851*, No. 156871.
(75) Li, S.; Yu, L. L.; Shi, Y. T.; Fan, J.; Li, R. B.; Fan, G. Di.; Xu, W. L.; Zhao, J. T. Greatly Enhanced Faradic Capacities of 3D Porous Mn 3 O 4 /G Composites as Lithium-Ion Anodes and Supercapacitors by C-O-Mn Bonding. *ACS Appl. Mater. Interfaces* **2019**, *11*, 10178−10188.
(76) Sun, X.; Wang, J.; Chen, B.; Dai, G.; Situ, Y.; Huang, H. High-Performance Adjustable Manganese Oxides Hybrid Nanostructure for Supercapacitors. *Electrochim. Acta* **2021**, *381*, No. 138213.
(77) Oyedotun, K. O.; Momodu, D. Y.; Naguib, M.; Mirghni, A. A.; Masikhwa, T. M.; Khaleed, A. A.; Kebede, M.; Manyala, N. Electrochemical Performance of Two-Dimensional Ti3C2-Mn3O4 Nanocomposites and Carbonized Iron Cations for Hybrid Supercapacitor Electrodes. *Electrochim. Acta* **2019**, *301*, 487−499.
(78) He, Q. Q.; Wang, H. Y.; Lun, N.; Qi, Y. X.; Liu, J. R.; Feng, J. K.; Qiu, J.; Bai, Y. J. Fabricating a Mn3O4/Ni(OH)2 Nanocomposite by Water-Boiling Treatment for Use in Asymmetric Supercapacitors as an Electrode Material. *ACS Sustainable Chem. Eng.* **2018**, *6*, 15688−15696.
(79) Sun, D.; He, L.; Lai, Y.; Lian, J.; Sun, J.; Xie, A.; Lin, B. Structure and Electrochemical Properties of Mn3O4 Nanocrystal-Coated Porous Carbon Microfiber Derived from Cotton. *Materials* **2018**, *11*, No. 1987.

https://doi.org/10.1021/acsomega.1c02302
ACS Omega 2021, 6, 31421−31434